International Journal of Impact Engineering 158 (2021) 103978

Contents lists available at ScienceDirect

International Journal of Impact Engineering

journal homepage: www.elsevier.com/locate/ijimpeng

A novel tests set-up for validation of connector models subjected to static and impact loadings

Matthias Reil [a,b,c], David Morin [b,c,*], Magnus Langseth [b,c], Octavian Knoll [a]

[a] BMW Group, Knorrstrasse 147, 80937 Munich, Germany
[b] Centre for Advanced Structural Analysis (CASA), NTNU, NO-7491 Trondheim, Norway
[c] Structural Impact Laboratory (SIMLab), Department of Structural Engineering, NTNU, NO-7491 Trondheim, Norway

A B S T R A C T

A novel test set-up is presented for validation of hybrid connector models between steel and aluminium components subjected to static and impact loading. The proposed components consisted of two hat profiles in steel and aluminium joined by adhesive bonding combined with self-piercing riveting. The geometry of the components was determined by numerical simulations in order to focus the behaviour on the connections under normal and shear dominated loading. The chosen components were tested under static and dynamic loading conditions in a 3-point bending setup. Different displacement measurement techniques were applied to reveal the specimens behaviour, including digital image correlation.Test results were applied to validate idealized numerical models of adhesive and self-piercing riveting connections.

1. Introduction

According to Oberkampf and Roy [1], the impact and capability of numerical simulations have the last 2–3 decades increased at an astounding pace and is now common design practice in industry. Thus, the use of numerical simulations has increased with regard to helping designers and project managers to improve their decision making, as well as in the assessment of safety and reliability of manufactured products and processes. During most of the revolution linked to the use of numerical simulations, the design of products and processes were based primarily on testing and engineering judgement, while numerical simulations were commonly a secondary contributor in both preliminary and final design. However, numerical simulations have now moved from a supporting role to a leading role in design.

The impact of numerical simulations relies on its credibility, i.e. that the results of an analysis are worthy of belief or confidence. The fundamental elements that build credibility is validation which is a process of assessing the physical accuracy of a mathematical model based on comparison between computational results and experimental data. A validation activity therefore requires access to high-quality experimental data in order to critically assess the computational results.

When modelling structures subjected to static and impact loadings, both the constitutive equations used to describe their materials as well as the models used to represent their connections must be validated. Up to now, a strong focus has been placed onto the validation of constitutive and fracture models for materials subjected to static and dynamic loading conditions [2, 3]. Validation of these models is usually carried out at two different levels, using material coupon tests [2] and using component tests [3]. Following this type of validation hierarchy, constitutive and fracture models can be properly assessed to ensure credible numerical simulations. While it is common to validate material models, the validation of numerical representation of connections, e.g., connector models [4, 5, 6, 7], is not well documented in the literature. One potential reason for this, is that common test set-ups like the crushing of double hat profiles end up focusing the loading on the base materials rather than the connections itself. Furthermore, the various joining techniques (self-piercing rivets [8], flow-drill screws [9] etc.…) available today and the potential range of materials (aluminium alloys [9], steels [10], CFRP [11] etc.…) make it difficult to build high-precision tests to support the validation of connector models.

In this context, the focus in the present work is to show how numerical simulations can be used to build a validation strategy for modelling of connections between steel and aluminium components subjected to static and impact loading using adhesive bonding combined with self-piercing riveting (SPR). As shown, for instance, by Sønstabø *et al.* [12] the validation of a connector model should be carried out at various levels where tests of varying complexity should be carried out. The first step in this study is to show how numerical simulations can be used to design components for precision testing as support for computer code validation. The chosen components are then tested under static and

* Corresponding author.
E-mail address: david.morin@ntnu.no (D. Morin).

https://doi.org/10.1016/j.ijimpeng.2021.103978
Received 23 February 2021; Received in revised form 12 June 2021; Accepted 21 July 2021
Available online 17 August 2021

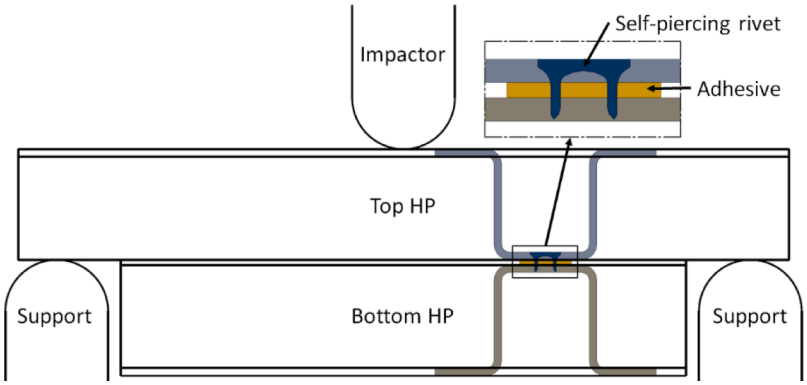

Fig. 1. Principle of the new component test for hybrid connections.

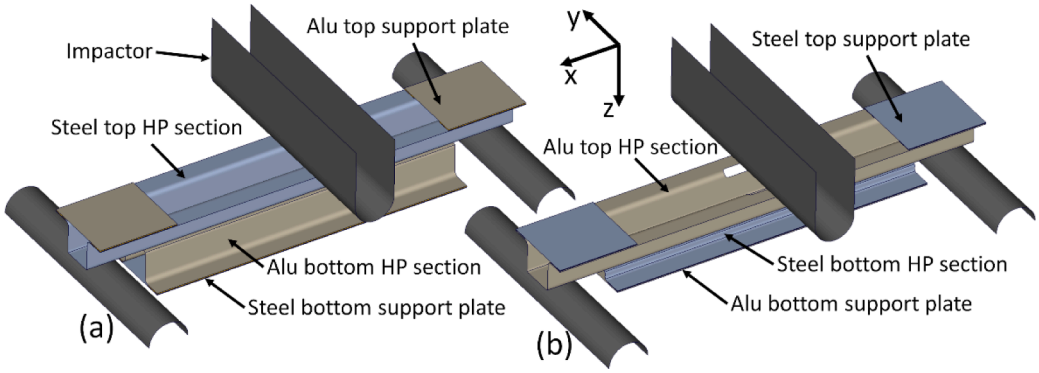

Fig. 2. Idealised model of the quasi-static component tests, a) normal and b) shear loading configuration.

dynamic loading conditions using up to date diagnostic techniques. Finally, the data generated from the experiments are used to validate connector models for adhesive and self-piercing rivets. The new and original scientific contribution of the present work lies in how the new test components are generated using numerical simulation for validation of connector models. It is believed that the proposed specimens and thus the validation approach shown is an important step for replacing expensive and time-consuming testing with reliable numerical simulations.

2. Design of components and fabrication

2.1. Geometry of the component test specimen

A novel test for hybrid connections between steel-aluminium components is proposed based on numerical simulations. Hybrid connections refer here to the combined application of adhesive bonding and SPR. The idea is to develop components in order to represent the main deformation modes present in a car body during a crash scenario and to focus the loading on the joining elements. In this context two Hat Profile (HP) sections are proposed as shown in Fig. 1 and joined for 3-point bending testing.

The well-defined boundary conditions of a 3-point bending setup ensures a simple correlation with numerical models. In addition, the SPR process requires access to the joining location from both sides which is enabled by the open geometry of the HP sections. The ten SPR connections are distributed evenly over the length of the bottom HP sections. The adhesive layer has a nominal width of 15 *mm* and a nominal thickness of 0.3 *mm*. One HP section is in steel grade CR380LA with a nominal thickness of 1.2 mm. The other one is in aluminium alloy AL6HYF with a nominal thickness of 2.5 mm. The HP sections are joined using the crash modified, hot curing epoxy adhesive SikaPower SP498 [13] and self-piercing rivets of type Böllhoff RIVSET 5.3 × 5 SKR.

2.2. Numerical design

Quasi-static Finite Element simulations were performed to optimize the proposed design of the component tests. The commercial code Abaqus/Explicit 2017–7 was used. Two simulation models were proposed as seen in Fig. 2 where the position and geometry of the aluminium and steel profiles relative to each other was varied. The set-up shown in Fig. 2a shows the steel profile at the top, whereas Fig. 2b shows the steel profile at the bottom. As will be explained later, the cause for this variation was linked to the wish of introducing several local deformation modes in the joints. The support plates were used to stiffen the specimens at the supports and thus prevent buckling of the top profiles.

In the numerical model the impactor and supports were represented by surface elements of type SFM3D4R [7] and modelled as rigid. The impactor was positioned with an offset of 15 mm to the middle plane between the supports to control the initiation of fracture in the adhesive. A velocity boundary condition was applied to the impactor in positive z-direction. During quasi-static simulations, a velocity of 10 mm/min was used in accordance with the experiments. Mass scaling was applied to reduce computation time. All degrees of freedom of the supports were constrained. Contact was handled by the general contact algorithm available in Abaqus/Explicit and a friction coefficient of 0.15 was used.

2.2.1. Modelling of the base materials

The steel and aluminium sheets were discretised with reduced integrated shell elements of type S4R [7] and five integration points in thickness direction. A mesh size of 2 mm was found to describe adequately the deformation behaviour. The isotropic, non-quadratic Hershey yield criterion [14] was applied to describe yielding and

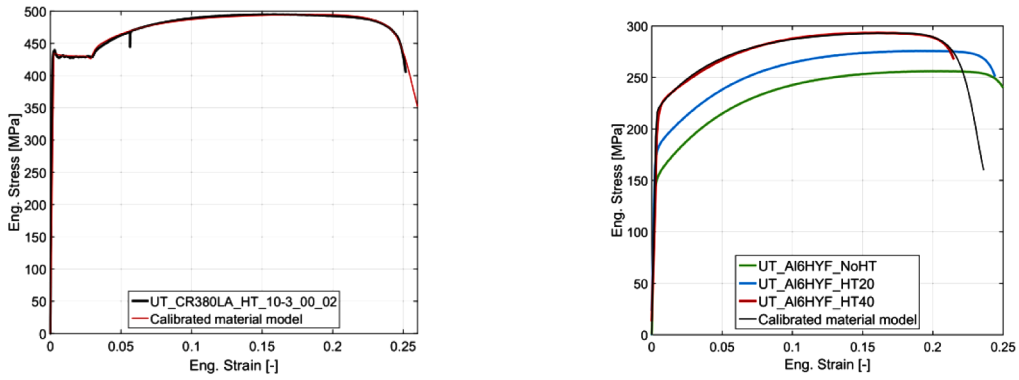

(a) CR380LA (b) AL6HYF

Fig. 3. Comparison of the representative UT test with the calibrated material model.

Table 1
CR380LA and AL6HYF material model parameters.

Parameter	Unit	CR380LA_HT	AL6HYF_HT40
E	[GPa]	210.0	70.0
ν	[-]	0.3	0.3
σ_y	[MPa]	436.0	210.0
a	[-]	6	8
p_{start}	[-]	0.026	0
Q_{R1}	[MPa]	15.8	9.2
θ_{R1}	[MPa]	9517.8	12,804.4
Q_{R2}	[MPa]	43.6	63.3
θ_{R2}	[MPa]	1477.0	1579.8
Q_{R3}	[MPa]	620.2	181.9
θ_{R3}	[MPa]	692.3	502.8

plastic flow, through an associated flow rule, of both the steel and aluminium alloys. Details on the applied material model can be found in Appendix A. A young's modulus of $E = 210GPa$ and $E = 70GPa$ were chosen for the steel and aluminium material, respectively while the Poisson's ratio was set to 0.3 for both materials. Model parameters defining the plastic behaviour were calibrated from Uniaxial Tensile (UT) tests through reverse engineering. The implicit solver of ABAQUS was employed for this purpose using a solid elements representation of the UT specimen. Reduced integrated elements C3D8R [7] were used to discretize the specimens with a mesh size of approximately 0.2 mm and 0.12 mm for the aluminium and steel alloy, respectively. The validity of the work-hardening parameters obtained with solid elements was evaluated in previous works of the authors (see Costas *et al.* [3]).

The components for testing were placed in an oven at 180 °C for 40 min to cure the adhesive. Thus, the influence of the curing cycle on the steel and aluminium material was investigated and taken into account into the numerical simulations. Test results on the UT specimens with different heat treatment had shown, that the curing cycle had no strong influence on the behaviour of the steel material. However, the curing cycle had a strong influence on the aluminium material as shown in Fig. 3b where representative tension tests without heat-treatment, 20- and 40-minutes curing cycles are shown. UT specimens were machined directly from the component specimens after curing for the calibration of the aluminium material model. The comparison between the calibrated material models and the representative UT tests for steel and aluminium is shown in Fig. 3. For aluminium the comparison is only shown for the 40-minutes curing cycle which is used in the subsequent numerical simulations. A good fit was achieved for both materials. An offset plastic strain $p_{start} = 0.026$ was defined for the steel material to account for the observed yield plateau.

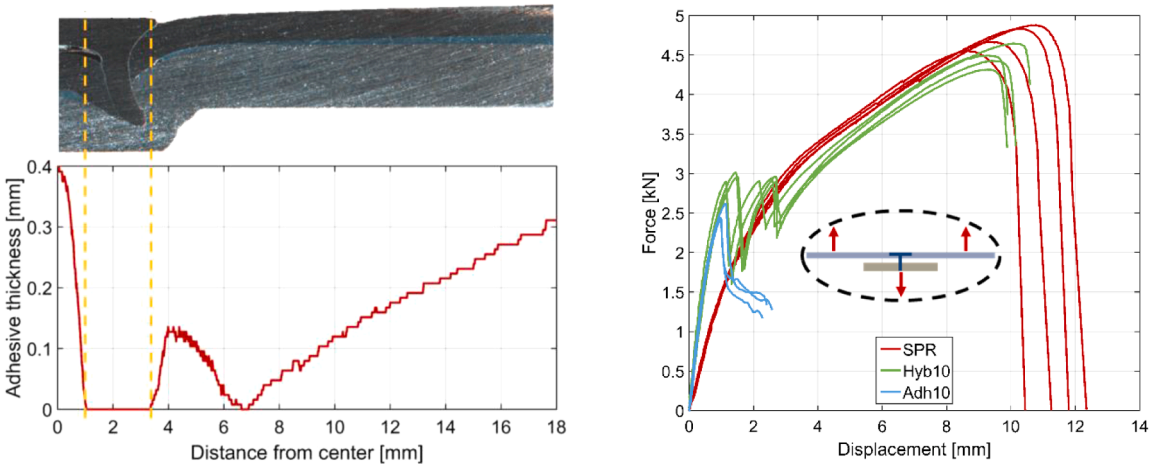

(a) Geometry and variation of the adhesive thickness (b) Force-displacement curves of cross-specimens under tension loading

Fig. 4. Effect of the adhesive on SPR connections.

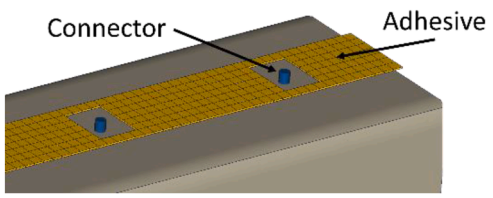

Fig. 5. Representation of the hybrid connection in the component test simulations.

Table 2
Calibrated parameters of the SPR connection model.

Parameter	Unit	Experimental calibration
E_n	[N/mm]	5000.0
E_s	[N/mm]	20,000.0
α	[1/mm]	0.18
β	[-]	1.25
R_N	[-]	4.8
R_S	[-]	7.4
F_y^{H0}	[N]	660.0
F_y^{H1}	[N]	880.0
F_y^{H2}	[N]	1000.0
$u_{pl.eq}^{H1}$	[mm]	6.0
$u_{pl.eq}^{H2}$	[mm]	16.0
$u_{pl.eq}^{I-Tension}$	[mm]	15.0
$u_{pl.eq}^{I-Mixed}$	[mm]	22.0
$u_{pl.eq}^{I-Shear}$	[mm]	23.0
$\Delta u_{pl.eq}^{I-Tension}$	[mm]	11.0
$\Delta u_{pl.eq}^{I-Mixed}$	[mm]	12.0
$\Delta u_{pl.eq}^{I-Shear}$	[mm]	32.0

The parameters of the calibrated material models are summarised in Table 1.

Since the HP sections were obtained by cold forming, the bending process of the HP sections was simulated and the equivalent plastic strain was mapped to the model of the component specimen. In this mapping procedure, it was further assumed that there was no interaction between the residual plastic strains due to the forming process and the change of material properties due to the curing cycle. For a more in-depth analysis of this potential interaction the reader is referred to, for instance, the work of Engler *et al.* [15].

2.2.2. Modelling of joints

In the current study, the adhesive is applied prior to the SPR and is in a liquid form until a curing cycle is applied. Fig. 4a shows the cross section of the hybrid connection together with the variation of the adhesive thickness. The adhesive was squeezed out entirely between 1 mm and 3.5 mm distance from the centre. This is where the rivet penetrated the top sheet. The presence of the adhesive had no significant impact on the SPR connection locally and had only minor impact on the strength and ductility of the SPR joints. This is demonstrated in Fig. 4b where the response under tension loading of a cross specimen with a hybrid joint (with adhesive and SPR, Hyb10) is compared to the same specimens without adhesive (SPR) and without SPR (Adh10). Therefore, it was chosen to exclude any interaction between the adhesive and the SPR in the numerical model. Following this approach, the adhesive was not taken into account in the calibration of the SPR connection model. The adhesive layer between the two HP sections and between the HP sections and the support plates was discretised with cohesive elements of type COH3D8 [7] and a mesh size of 2 mm. The cohesive elements were connected to the shell elements of the steel and aluminium by tied constraints therefore precluding the potential interfacial fracture between the adhesive layer and the metallic materials. The adhesive layer connecting the top and bottom HP section had a width of 15 mm.

According to the distribution of adhesive around the SPR connection (Fig. 4a) gaps were introduced around the Rivet, Fig. 5, to account for the chosen non-interaction behaviour.

The behaviour of the adhesive was described by a triangular traction-separation law and details about this cohesive zone model is described in Appendix B. Crack propagation in the adhesive layer was modelled by successive deletion of cohesive elements. The material parameters applied in this work were taken from the IGF research project 422 ZN [16]. This project used the same adhesive as in this study.

The Abaqus fastener formulation [7] was applied to represent the macroscopic behaviour of the SPR connections. Here, a three dimensional two-nodes connector element (CONN3D2) is placed in between the connecting surfaces. Nodes of all shell elements that are within a user defined radius r_{rof} from the fastening points are part of the coupling nodes. Translations and rotations of the respective fastening points are coupled to the average translation. A radius of influence of $r_{rof} = 7.0mm$ was found to represent the connection behaviour adequately in terms of stiffness while accounting for the effect of the SPR onto the joining partners (see Fig. 4a).

A detailed elaboration of the applied connector model can be found in Appendix C. Parameters of the outlined connector model were calibrated by a reverse engineering approach and are summarized in Table 2.

The new cross test rig introduced by Sønstabø *et al.* [9] was applied to

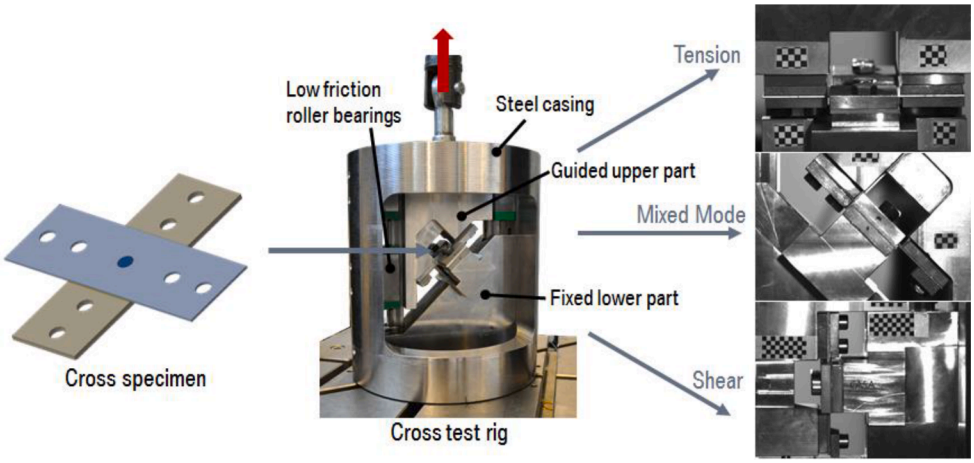

Fig. 6. Test setup used to establish the mechanical behaviour of SPR connections.

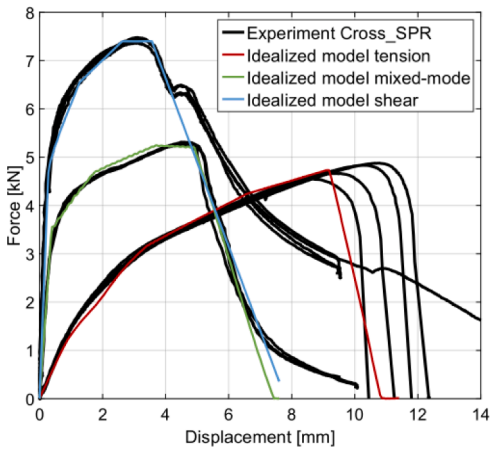

Fig. 7. Comparison between cross test experiments and calibrated SPR connection model.

test connections under tension, shear and mixed mode loading, Fig. 6.

Parameters of the connector model were chosen to match the recorded force-displacement responses of riveted cross specimens under different loading modes, Fig. 7. The experimental data was obtained for the same material combination as in the component test following the same curing cycle. The chosen fastener formulation was able to represent the behaviour of the riveted cross specimen accurately. Under shear loading, the rivet was jammed in between the top and bottom sheet which resulted in a slower force reduction after failure (after roughly 4 mm in Fig. 7). The jamming of the rivet is caused by the strong constraints imposed by the cross-test rig under shear loadings. It is assumed that this phenomenon is not representative for fracture in shear in structural applications and the connector model was therefore not calibrated to represent this behaviour.

2.2.3. *Component test design*

The geometry of the HP sections relative to each other determined the deformation mode of the combined adhesive and self-piercing rivet connections. Therefore, two configurations were tested out, one for normal and one for shear dominated loading.

In the normal loading configuration, Fig. 8a, the top and bottom HP sections in steel and aluminium respectively, had the same height. As seen in Fig. 8a, the top HP section was bent for increasing impactor displacement, whereas the bottom HP section remained straight. This resulted in a relative displacement normal to the connected surfaces and thus introduced a tension load in the connections. Considering the offset of the impactor with respect to the middle plane of the specimen, fracture took place in four self-piercing rivets (indicated in Fig. 9a by numbers) while the remaining six SPR connections did not experience fracture.

In the shear loading configuration, Fig. 8b, the height of the bottom HP section in steel was significantly reduced which lowered the bending stiffness of this profile compared to the normal loading configuration. The relative displacement between the connected members was now tangential to the connected surface, resulting in a shear dominated loading. Failure in the connection was triggered from one side due to the offset of the impactor. As for the normal loading configuration, four SPR connections experienced fracture while the remaining six SPR

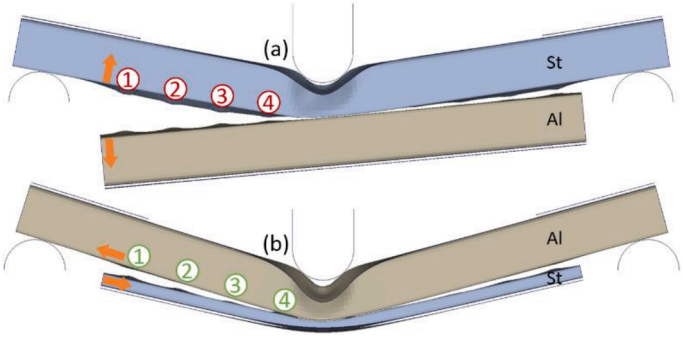

Fig. 8. Bending behaviour of the normal (a) and shear (b) loading configuration.

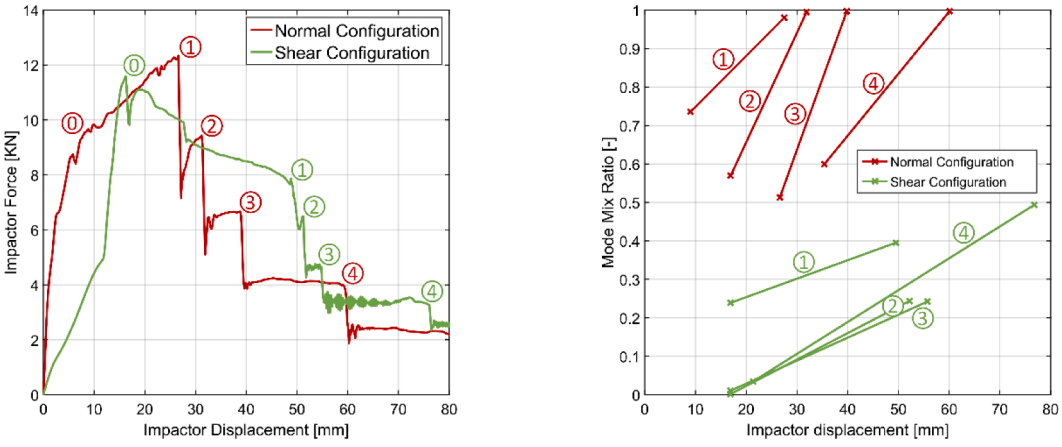

Fig. 9. Predicted behaviour of a) the normal and b) shear loading component.

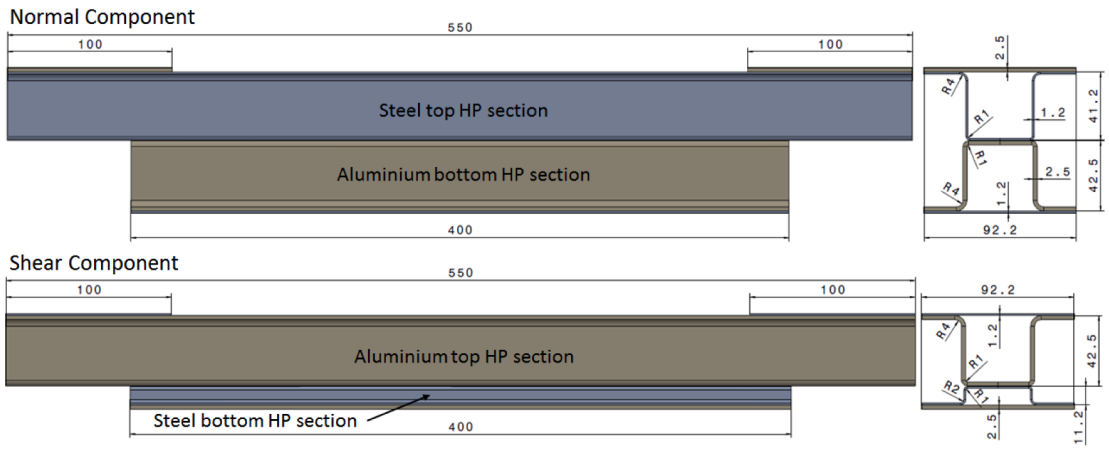

Fig. 10. Component test specimen geometry.

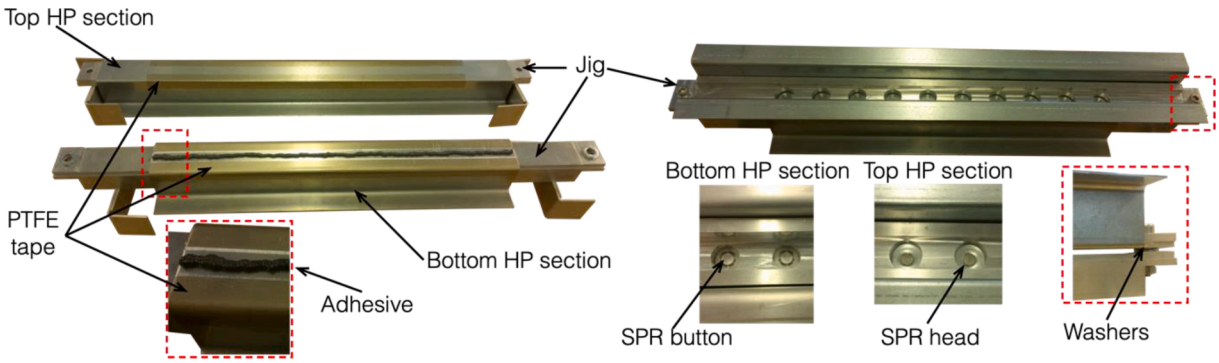

Fig. 11. Joining of the component test specimens.

connections were still intact at the end of the analysis.

The force-displacement response of the normal (red) and the shear loading configuration (green) is shown in Fig. 9a where it can be observed that a successive failure of four SPR connections was predicted for both specimen configurations. The loading mode of SPR connections can be assessed quantitatively by studying the mode-mix ratio Ψ_m of the connector elements, Equation C.6, which translates the amount of tension and shear forces transferred through the connections. The mode-mix ratio Ψ_m takes a value of 1 for pure tension loading and 0 for a pure shear loading. Fig. 9b shows the mode-mix ratio Ψ_m versus the impactor displacement of the four critical SPR connections for both the normal (red) and shear (green) loading configurations. The mode-mix ratio was extracted at the onset of plastic deformation and at failure of each connection. Here, a value above 0.5 indicated normal dominated loading while a value below 0.5 indicated shear dominated loading. In the normal loading configuration, the mode-mix ratio was mostly in the region above 0.5. The loading mode changed from normal dominated mixed-mode loading to almost pure normal loading between the onset of plastic deformations and connection failure. In contrast, the mode-mix ratio stayed below 0.5 in the shear loading configuration. Here, plastic deformations of the connectors were initiated under almost pure shear loading. Connection failure occurred under shear dominated and mixed-mode loading. Failure of SPR connections resulted in a significant drop of the impactor force for both specimen configurations. In the normal loading configuration, failure of SPR connections were distributed between an impactor displacement of 26 mm and 60 mm. The failure sequence in the shear loading configuration started at a significantly higher impactor displacement and occurred more rapidly, three of the SPR connections failed within a 10 mm interval. In this loading scenario, the tangential relative displacement (i.e. shear) means that the load is distributed more evenly over the whole specimen. Failure of the adhesive layer was initiated before the failure of the first SPR connection for both loading configurations as indicated by the markers 0 in Fig. 9a.

2.3. Specimen manufacturing

The final specimen geometry of the normal and shear loading configuration generated from the numerical design optimisation is shown in Fig. 10.

The HP sections were bent from CR380LA steel sheets with a nominal thickness of 1.2 mm and AL6HYF aluminium sheets with a nominal thickness of 2.5 mm. The support plates were machined from the same material. A jig was designed for joining of the HP sections to ensure an accurate positioning of the Rivets as well as the relative positions of the top and bottom HP sections. Fig. 11 shows the jig used in this study.

A thin PTFE tape was applied to the bonding surface of the steel and aluminium HP section to control the width of the adhesive layer to 15 mm (Fig. 11). To improve the quality of the bonding, all bonding surfaces were cleaned with isopropanol to remove any traces of oil contamination.

The HP sections were then placed onto the two parts of the joining jig (Fig. 11). Here, the grooves in the joining jig match the length of the HP sections to ensure an accurate positioning. A thin line of adhesive was applied onto the bottom HP section with a hand driven adhesive application gun (Fig. 11). The top HP section together with the jig was then placed on top of the bottom part (Fig. 11). The top and bottom part of the joining jig were assembled by bolts and nuts on the left and right side. The adhesive was squeezed in between the HP sections by tightening of the bolts. Steel washers were placed between the top and bottom part of the joining jig to control the thickness of the adhesive layer and ensure an even distribution (Fig. 11).

To obtain an accurate positioning of the ten SPR connections, holes

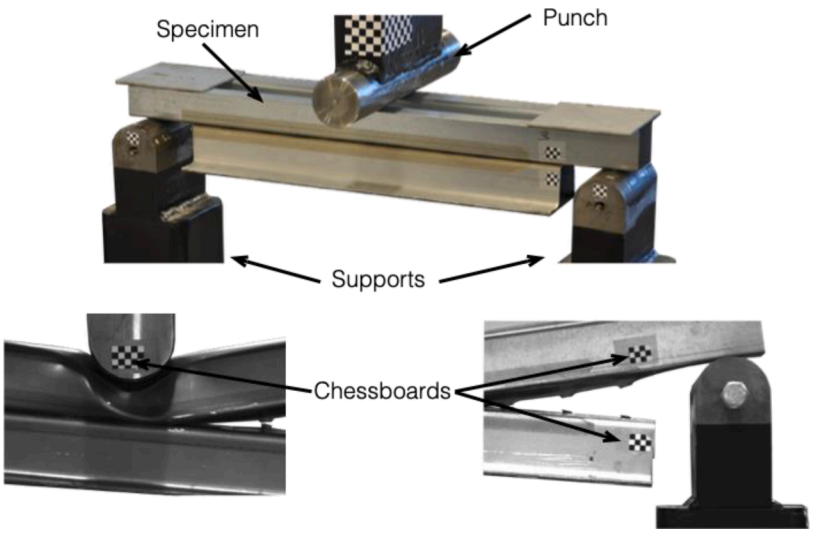

Fig. 12. Quasi-static component test set-up.

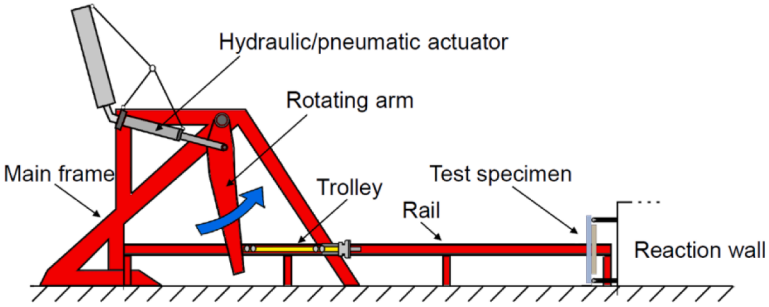

Fig. 13. Principle of the pendulum impactor test after [19].

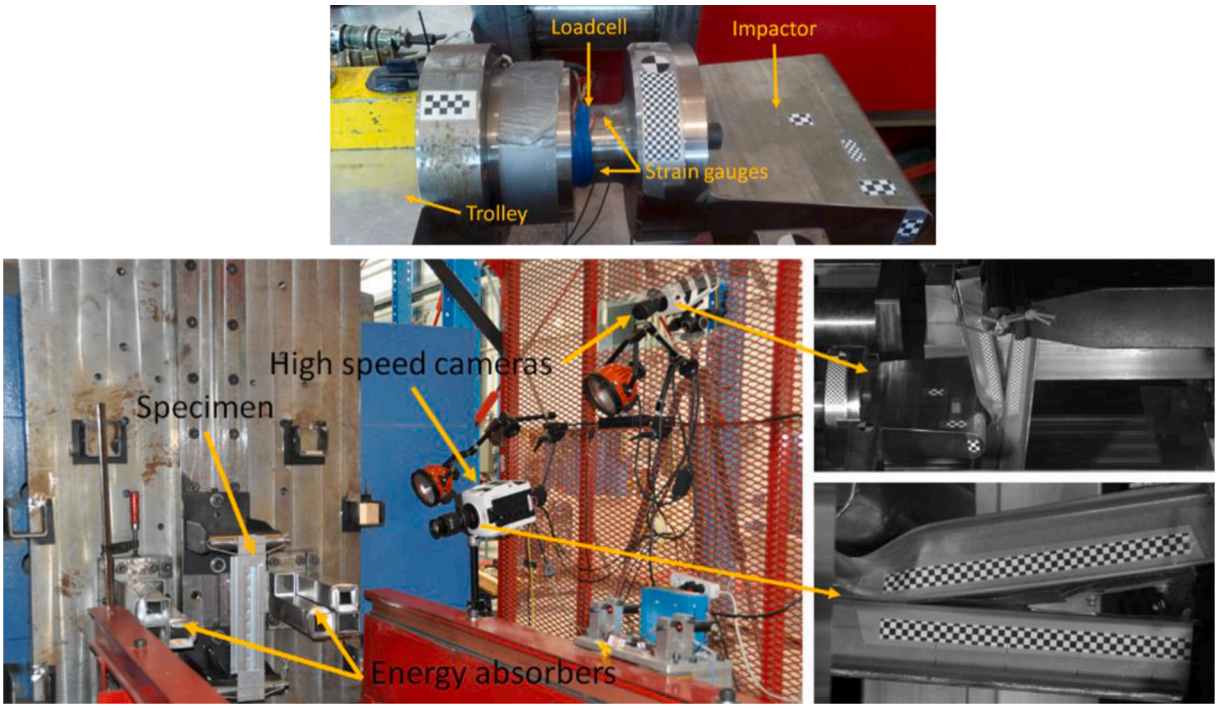

Fig. 14. Dynamic component test set-up and force measurements.

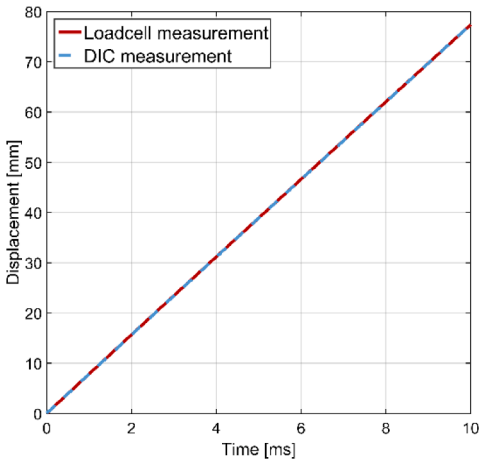

Fig. 15. Comparison of the applied displacement measurements.

in the joining rig corresponding to the outer diameters of the riveting die and blank holder were manufactured (see Fig. 11). After joining, the component test specimen was then removed from the joining jig. At this stage, the SPR connections kept the top and bottom HP section securely in place. Finally, the support plates were bonded onto the flanges of the top and bottom HP section and the specimens were cured inside an hot air oven at 180 °C for 40 min.

3. Experimental set-up

3.1. Quasi-static component tests

Quasi-static experiments were performed using an electromechanical dual column testing machine with a capacity of 250 kN. The normal and shear specimens were placed between a moveable punch and fixed supports as shown in Fig. 12.

The punch and supports had a radius of 25 mm and were both made from steel. The distance between the supports was 500 mm. The impactor was positioned with an offset of 15 mm to the centre plane between the supports. All tests presented in Section 5.1 and 5.2 were carried out without any lubricant in between the specimen and the impactor/supports. The effect of friction was evaluated with a series of normal loading tests with additional PTFE plates at the supports and under the impactor and a negligible effect of friction was found. All experiments were performed at a constant impactor velocity of 10 mm/min. A camera system was used to track the impactor displacement and the relative movement of the HP sections. For that purpose, chessboard patterns were applied to the impactor and the specimens as shown in Fig. 12 and the in-house DIC-software eCorr [17] was used to measure the required displacements.

3.2. Dynamic component tests

Dynamic component tests were carried out using a pendulum impactor as depicted in Fig. 13. The reader is referred to Hanssen *et al.* [18] for more information on the test rig.

A trolley with a mass of 400 kg was accelerated by a hydraulic/pneumatic actuator system. The trolley was guided on rails towards the test specimen. A steel impactor with a radius of 25 mm was mounted to the front of the trolley. The test specimen was placed onto steel supports with a radius of 25 mm (the radius of the impactor and supports were the same as for the quasi-static tests). The steel supports were bolted to the reaction wall. Here, an offset of 15 mm between the centre plane of the impactor and supports was applied in accordance with the quasi-static tests. A nominal impactor velocity of 8.0 m/s was chosen. The remaining kinetic energy of the trolley after deforming the test specimen was absorbed by aluminium buffers consisting of profiles. These buffers were mounted to the left and right side of the test specimen. The force was measured by a load cell mounted between the trolley and the impactor as shown in Fig. 14. A total of four strain gauges were mounted on the circumference of the load cell. The strain gauges were connected by a wheatstone bridge. The load cell was calibrated using a universal testing machine to correlate the voltage signal from the strain gauge circuit to the force. Two high speed cameras with a frame rate of 25.000fps were applied in the dynamic tests as shown in Fig. 14. One camera recorded the displacement of the impactor. Chessboard patterns were applied to the impactor for that purpose. The second camera recorded the opening of the two HP sections to identify connection failure.

Chessboard patterns were applied to the top and bottom HP section to track the relative movements between both parts throughout the dynamic tests. The impactor displacement was not only established from the high-speed images, but also calculated from the measured force-time curve from the loadcell as follows

$$\boldsymbol{U(t) = V_0 t - \iint \frac{F(t)}{m} dtdt}$$

The two displacement measures were compared to study their accuracy and verify the data. An excellent agreement between the displacement measurements was found as shown in Fig. 15 thus ensuring the validity of the dynamic experiments.

4. Experimental results and discussion

4.1. Quasi-static component tests

Component tests were performed on the fabricated normal and shear specimen configurations. Here, the main objective was to generate experimental data for validation of numerical models of SPR and adhesively bonded connections. Thus, any material failure in the aluminium and steel components composing the specimens which could influence the local joint behaviour was not wanted.

Preliminary component tests were performed to ensure that the desired deformation and failure behaviour was achieved. In the normal loading configuration, no material failure was observed. However, in the shear loading configuration, fracture occurred in the bend of the aluminium top HP section right underneath the punch. The HP sections were manufactured from steel and aluminium sheets and the material in the radii of the HP sections was affected by the bending process. Here, work hardening from the manufacturing process resulted in a reduced ductility of the material. Slots were added in the critical areas of the aluminium top HP section to avoid material failure. A slot position and geometry as shown in Fig. 16 was found sufficient to avoid material failure in the aluminium components designed for shear loading joint behaviour.

The results of the quasi-static tests for the normal loading component are shown in Fig. 17. The force increased linearly up to the point where the top HP section started to deform plastically underneath the impactor and buckling took place in the side wall (Fig. 17a). At position 0 in the force-displacement curve, a crack was initiated inside the adhesive layer from the left edge. The crack propagated towards the first SPR connection for increasing impactor displacement (Fig. 17b). The maximum force was reached right before failure of the first SPR connection at position 1 in the force-displacement curve (see also Fig. 17c). The crack inside the adhesive layer propagated towards the centre of the specimen for increasing displacements accompanied by successive failure of three more SPR connections at positions 2 to 4 (Fig. 17d). Failure of each SPR connection could clearly be identified by a significant drop in the force level. The repeatability of the experiments was excellent because of the accurate assembly process used. The steel top HP section was bent significantly, whereas the aluminium bottom HP section remained straight as planned during the design phase of this component test. Therefore, opening of the HP sections occurred normal to the joint

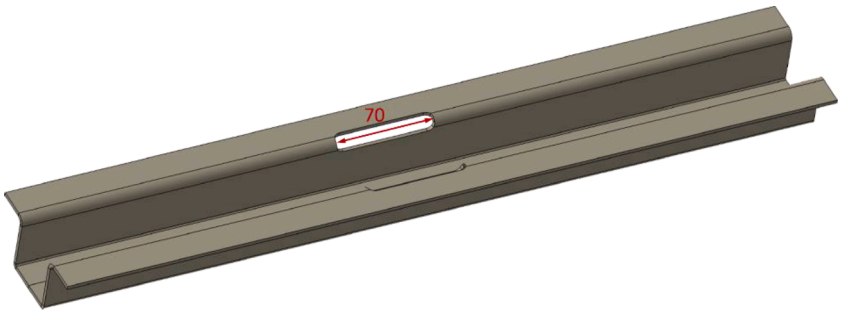

Fig. 16. Slot geometry of the shear loading component.

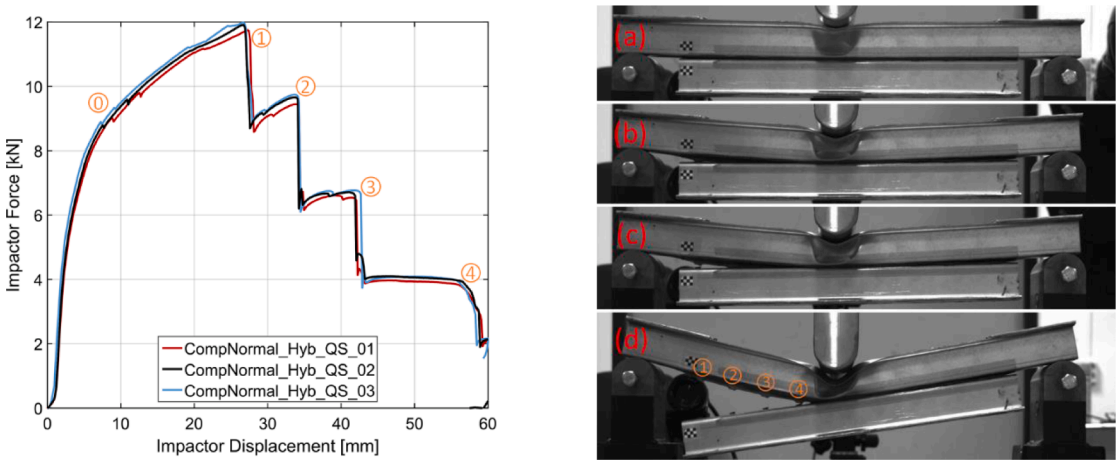

Fig. 17. Results of the normal loading component under quasi-static loading.

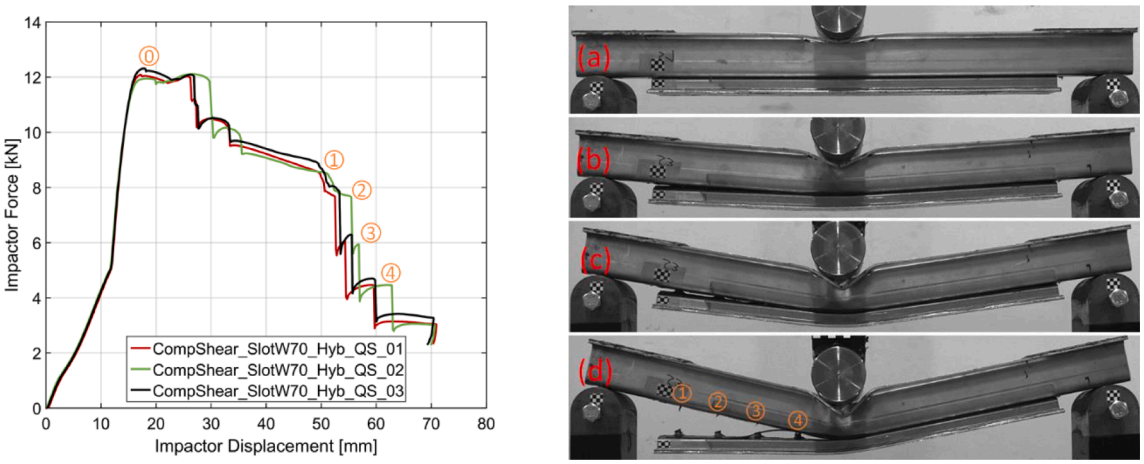

Fig. 18. Results of the shear loading component under quasi-static conditions.

surface and the adhesive and SPR connections were loaded in tension. This is confirmed by the deformation and failure behaviour of the SPR connections. The steel sheet was pulled over the rivet head and the rivet remained stuck in the aluminium sheet in a pull-over mode. Local deformations in the steel sheet were symmetrical around the rivet axis. Hence, the connection was loaded normal to the joint surface. The observed failure behaviour of the SPR connections was in good agreement with the predicted connector mode-mix ratios.

The force-displacement response of the shear loading component under quasi-static conditions is shown in Fig. 18.

Initially, the impactor was only in contact with the flanges of the top aluminium HP section and the force increased slowly. The impactor touched the side walls of the aluminium top HP section at approximately 11 mm displacement due to the introduced slots and the force increased with a higher slope, Fig. 18a. Subsequently, the side walls started to deform underneath the impactor, Fig. 18b, and failure was initiated inside the adhesive on the left side (indicated by position 0 in the force-displacement curve). Both mechanisms contributed to the force plateau at 12 kN. The crack in the adhesive propagated towards the centre of the specimen for increasing impactor displacement. Fig. 18c shows the shear specimen at approximately 50 mm displacement just before failure of the first SPR connection. In total, four SPR connections failed successively marked by positions 1 to 4, Fig. 18d. The loading was distributed more evenly over the SPR connections compared to the normal loading

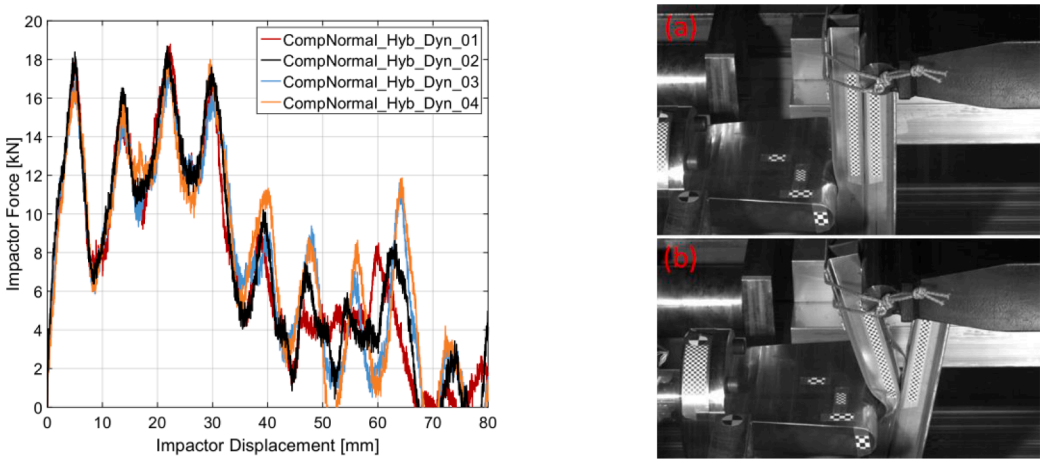

Fig. 19. Results of the normal loading component under dynamic conditions.

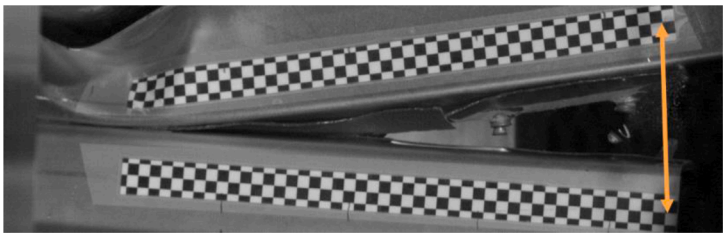

Fig. 20. Extraction of the HP section opening velocity.

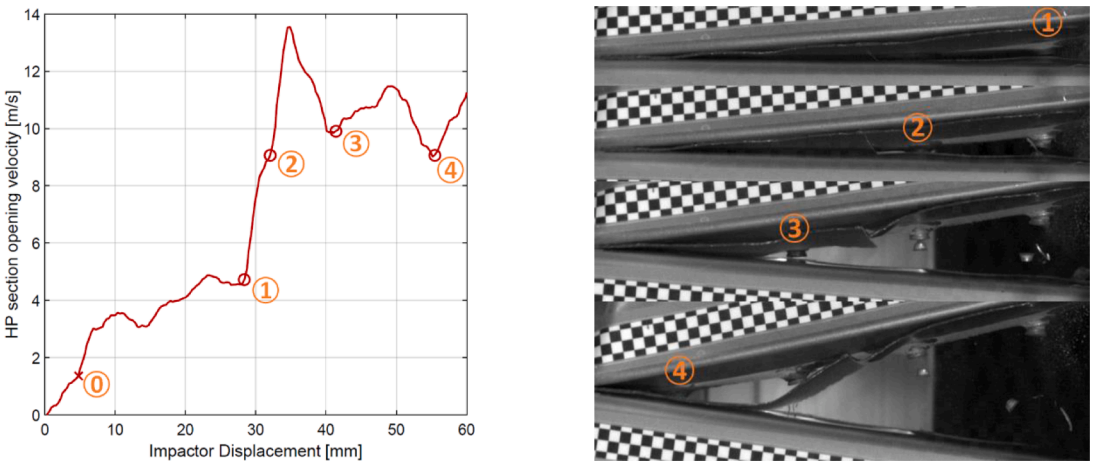

Fig. 21. Failure displacement extraction of the normal loading component under dynamic loading.

configuration. As a result, the four SPR connections failed within an impactor displacement of only 10 mm in the shear loading configuration compared to 30 mm in the normal loading configuration. Consequently, SPR connection failure started at a higher displacement but occurred in shorter succession. The slots machined in the aluminium top HP section allowed the side walls to deform without any material failure. The reduced height allowed the bottom HP section to follow the bend of the top HP section. Therefore, a shear dominated loading was introduced into the SPR connections as predicted by the simulations. Due to the shear dominated loading, the failed rivets experienced, locally, large rotations and were pulled out from the aluminium sheets in a pull-through mode.

4.2. Dynamic component tests

Results of the dynamic tests on the normal loading components are shown in Fig. 19.

Four repetitions were performed in total. A maximum force of approximately 18 kN was reached in all tests. First, the top HP section deformed plastically underneath the impactor and a crack was initiated inside the adhesive, Fig. 19a. The force level dropped significantly after approximately 35 mm displacement indicating failure of the SPR connections. A total of four SPR connections failed, triggered from one side, Fig. 19b. Their failure behaviour was tension dominated and the deformation mode was comparable to the quasi-static tests. The shape of the force signal was dominated by oscillations with an amplitude of roughly 6 kN and a frequency of approximately 900 1/s. They originated from the specimen which started to oscillate according to its

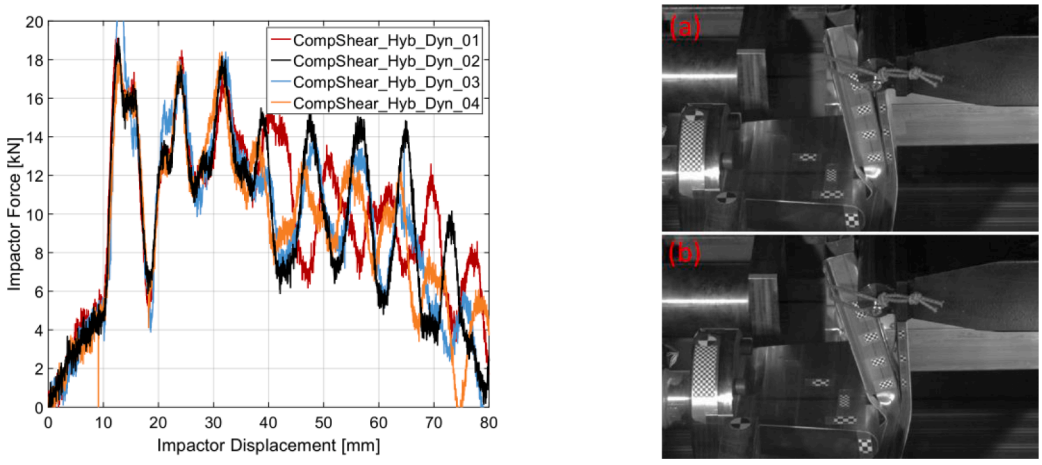

Fig. 22. Results of the shear loading component under dynamic conditions.

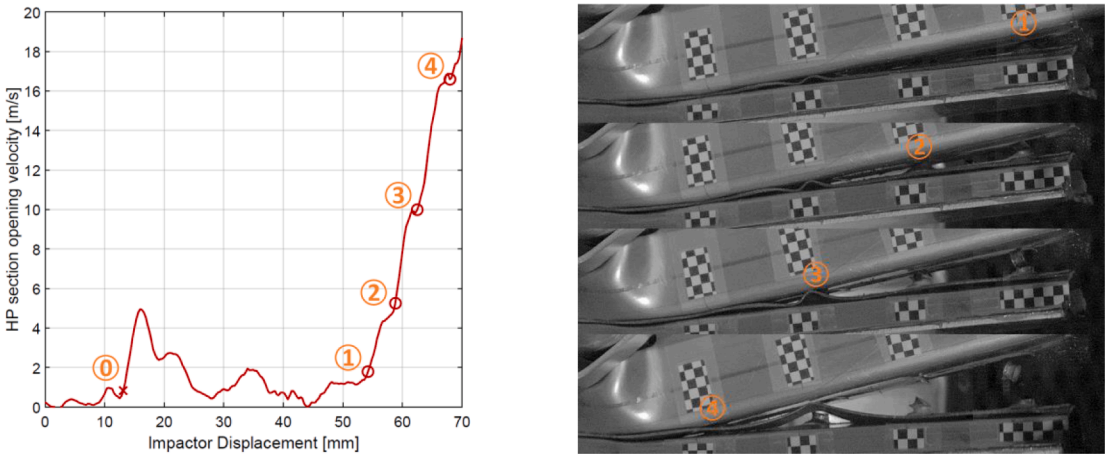

Fig. 23. Failure displacement extraction of the shear loading component under dynamic loading.

eigenfrequency. The oscillations impeded a direct identification of connection failure from the force signal. Thus, the high-speed camera images of the HP sections opening were used to identify connection failure. Chessboard patterns applied to the top and bottom HP sections allowed to calculate the relative opening velocity as depicted in Fig. 20.

Fig. 21 shows the HP sections opening velocity as a function of the impactor displacement for a chosen representative test.

The opening velocity increased slowly as the impactor hit the specimen. The first change in the opening velocity was observed at approximately 4 mm displacement. Here, failure was initiated inside the adhesive layer at position 0. A more pronounced change in the opening velocity occurred when the first SPR connection failed at position 1. The second SPR connection failed shortly after at position 2 and the opening velocity reached its maximum of approximately 13.5 m/s at a displacement of 35 mm. Subsequently, the velocity was reduced until failure of the third SPR connection at position 3. The opening velocity dropped after a moderate increase from position 3. The opening velocity increased again after failure of the fourth SPR connection at position 4. The identified connection failure points obtained from the opening velocity measurements were verified qualitatively from the corresponding high-speed camera images and a good agreement was found. It is interesting to note that even if the impact velocity was 8 m/s, the loading velocities at the joint level are varying significantly from the fracture of the first SPR connection to the three remaining SPR connections. On the opposite of the quasi-static tests, the failure mode of the rivets varied across the component with a mix of pull-through and pull-over modes.

The force-displacement response of the shear loading component specimen under dynamic conditions is shown in Fig. 22. Here again oscillations were found due to dynamics in the specimen.

The same methodology as for the normal loading component was applied to identify the exact moment of connection failure, see Fig. 23. Initially, forces increased slowly due to the slots in the top HP section up to a displacement of 10 mm. Subsequently, the force level increased rapidly as the impactor hit the side walls in the slots and a maximum force of approximately 18 kN was reached. The specimen bent for increasing displacement and the side walls of the top HP section started to buckle, Fig. 22a. As a result, the force level decreased gradually. Failure occurred inside the adhesive layer and at four SPR connections, which failed in the same mode as in the quasi-static component tests, Fig. 22b. No material failure occurred inside the HP sections before connection failure.

5. Comparison between component tests and simulation

The established numerical model of the specimens in Chapter 3 (used to design the specimens), is now compared with the quasi-static and dynamic component tests. The comparison will have a focus on the measured force-displacement curves including the displacement when rivet failure took place as well as the energy absorption in the components. Even if the numerical model was used to design the specimens, the comparison shown is a validation of the chosen model methodology for

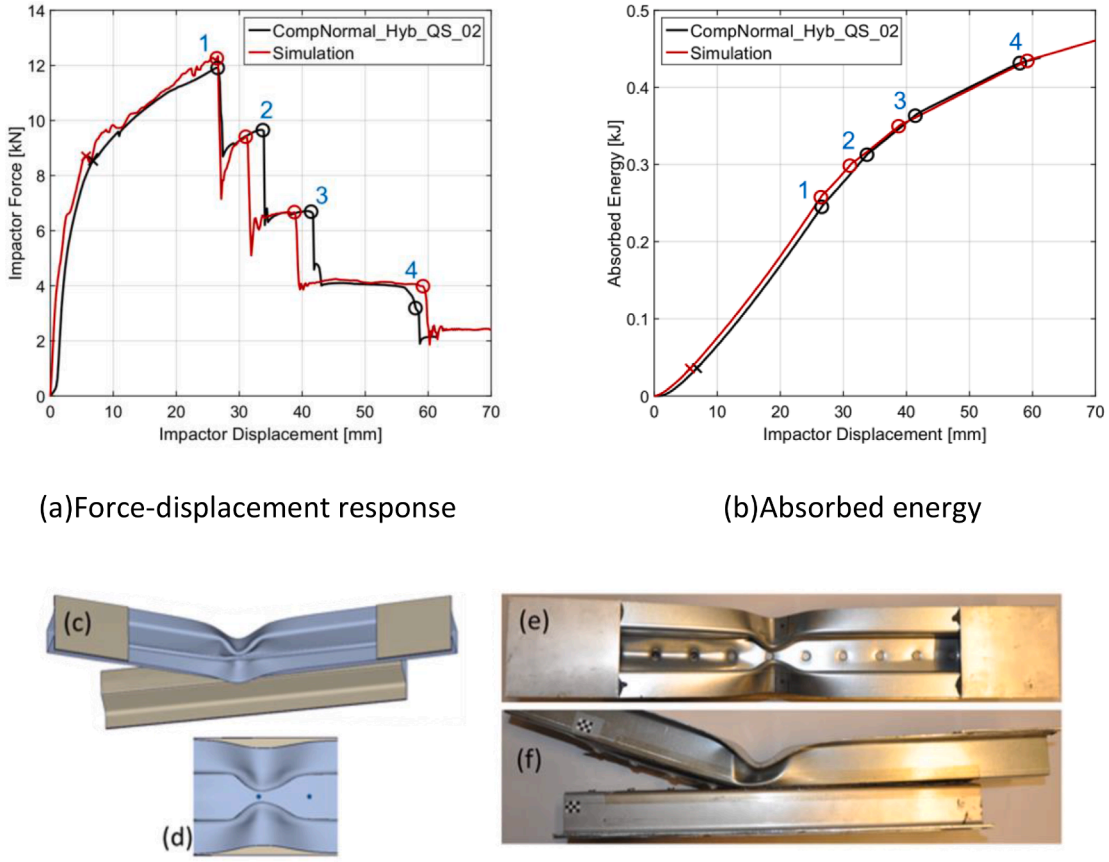

Fig. 24. Comparison of the quasi-static tests on the normal loading component.

large scale simulations.

5.1. *Quasi-static component tests*

Fig. 24 compares the experimental response of a representative quasi-static test on the normal loading component and its numerical counterpart. In overall, the numerical predictions of the global force-displacement and energy absorption curves (Fig. 24a and b) are in good agreement with the experiments obtained in Section 5.1. The final experimental and simulated deformed shapes of the normal loading component were also in good agreement (Fig. 24c-f).

The crosses in Fig. 24a and b indicate crack initiation inside the adhesive, while the circle represents failure of the SPR connections. The failure of the first cohesive elements was initiated from the left side because of the impactor offset. For increasing impactor displacements, the crack propagated further on the left side, but adhesive failure was also initiated on the right side as in the experiments. The behaviour of all SPR connections was predicted well by the applied connection model. A total of four connector elements failed successively from the left side. As in the experiments, no connector elements failed on the right side of the normal loading component. The force level at failure of each SPR connection was represented well by the simulation as well as the displacement.

Fig. 25 shows the response of the numerical simulation compared to a representative quasi-static test under shear dominated loading.

Overall, the force-displacement curve was represented quite well in the simulation, even if the force level was somewhat underestimated. The response up to crack initiation inside the adhesive was represented well by the simulation (marked by crosses in Fig. 25a and b). Failure of the first cohesive elements defined the maximum force in the simulation which was slightly lower compared to the experiment. In the experiment, crack propagation inside the adhesive occurred under an almost constant force level up to a displacement of approximately 28 mm. In the simulation, the force was noticeably lower, but following the same trend. The adhesive layer between the top and bottom HP section of the shear loading component was predominantly loaded in shear. Other researchers [20, 21] suggested the application of a trapezoidal traction separation law to describe the behaviour of ductile epoxy adhesives, especially under mode II loading. It is therefore assumed, that the applied triangular shape contributed to a lower force level in the simulation observed between 16 mm and 28 mm displacement. The cohesive law shape had less impact on the simulation of the normal loading component as here the adhesive layer was primarily loaded in peel. At approximately 28 mm displacement, the crack inside the adhesive layer reached the centre of the specimen and the force dropped accordingly. With increasing deformation, the force reduced gradually in the simulation as in the experiment up to failure of the first SPR connection. The displacement of the punch, when subsequent failure of the rivets took place, was represented quite well. However, the force level was somewhat underestimated giving a lower energy absorption compared to the tests. As indicated in Fig. 25c-f the final deformation shape was also predicted with reasonable accuracy.

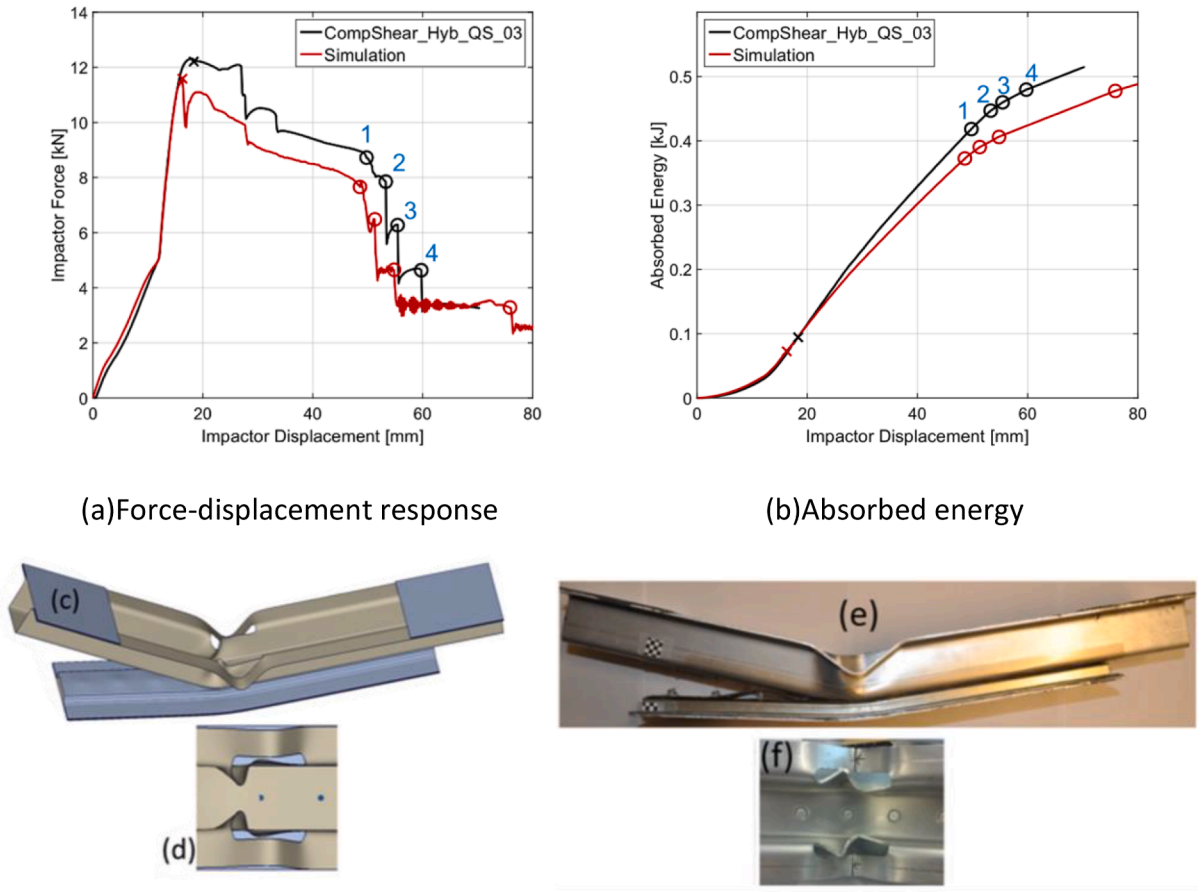

Fig. 25. Comparison of the quasi-static tests on the shear loading component.

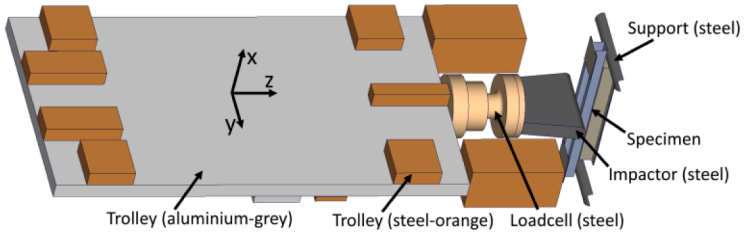

Fig. 26. Simulation model of the dynamic component test.

5.2. *Dynamic component tests*

5.2.1. *Numerical set-up*

Fig. 26 shows the model applied to simulate the dynamic component tests.

Specimen and supports were modelled according to the simulation model of the quasi-static tests, outlined in Section 2.2. Simulations were thus carried out with same model parameters as for the quasi-static simulations and any rate effects in the adhesive, SPR model as well in the steel and aluminium material were excluded. The simulations will thus only give a qualitative comparison with the impact tests carried out. It has to be mentioned that the flow stress of the aluminium material can be considered rate independent [22] and the steel used have a rather low strain rate sensitivity [23]. To establish rate dependant models for the adhesive and for the SPR model including calibration procedures were not a part of the scope of the present work.

Impactor, load cell and trolley were discretized with 8-node linear solid elements with reduced integration (Abaqus type C3D8R [7]). Impactor, load cell and parts of the trolley were made from steel. Their behaviour was modelled as linear elastic with a Youngs modulus of 210.0 GPa and a Poisson's ratio of 0.3. The other portion of the trolley was made from aluminium. Here, a Young's modulus of 70.0 GPa and a Poisson's ratio of 0.3 was applied. The general contact algorithm with a friction coefficient of 0.15 was used to model contact between impactor, specimen and supports. Impactor, load cell and trolley were connected by tied constraints. In accordance with the experiments, an initial velocity of 8.0 m/s was applied to the impactor, load cell and trolley in positive z-direction. The force was obtained from the load cell at the same location as the strain gauges in the experiment, see Fig. 14, by integrating the stresses over the cross-section area.

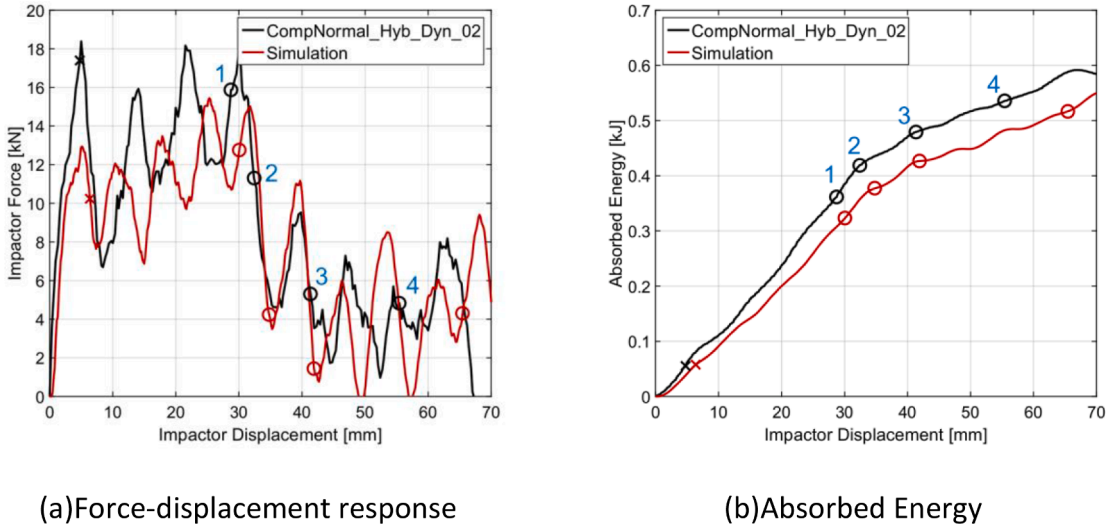

Fig. 27. Results of the normal loading component under dynamic conditions.

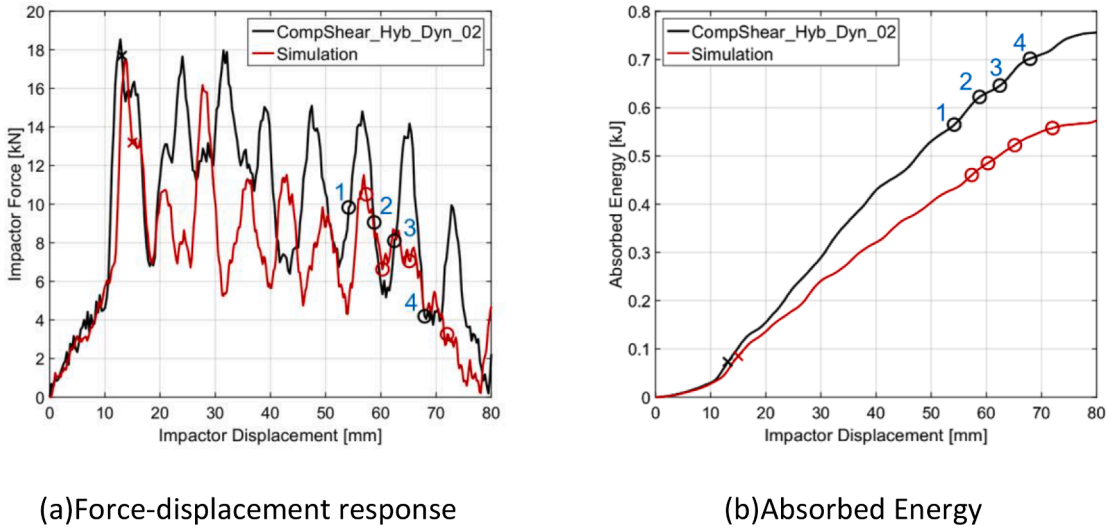

Fig. 28. Results of the shear loading component under dynamic conditions.

5.2.2. Comparison between simulation and experiments

Fig. 27a compares the force-displacement response of the normal loading component under dynamic loading.

A representative experiment is highlighted in black, while the simulation curve is highlighted in red. The initial stiffness was comparable. In the simulation, damage in the adhesive started at approximately 10.4 kN, but no cohesive elements were deleted. The force continued to increase with reduced stiffness and reached a maximum of approximately 13 kN before failure of the first cohesive elements took place marked by the cross. The corresponding maximum force in the experiment was significantly higher. The impactor displacement at failure initiation was however comparable. The force in the simulation remained below the experimental level up to failure of the first riveted connection. The absorbed energy at that point was approximately 11% smaller in the simulation compared to the experiment, Fig. 27b. The force level dropped after failure of the first riveted connection at approximately 30 mm displacement in both the simulation and the experiment. Subsequently, the force-displacement curves were in better agreement. The failure displacement of rivet number one to three was predicted well by the simulation whereas failure of rivet number four occurred at a noticeably higher displacement compared to the experiment.

Fig. 28a compares the force-displacement response of the shear loading component.

The force level was again noticeably lower in the simulation. However, the initial force peak before failure initiation inside the adhesive was in better agreement than for the normal loading component. Fig. 28b compares the absorbed energy of the shear loading component under dynamic conditions. Here, the energy absorbed up to failure of the first SPR connection was underestimated by approximately 19% in the simulation. The absorbed energy of the shear loading component under quasi-static conditions was also underestimated. It is assumed, that friction and the representation of the adhesive also affected the behaviour under dynamic loading. Despite the lower force level in the simulation, the displacement when connection failure took place was represented well.

Overall, the simulations were not able to accurately describe the dynamic behaviour of the normal and shear loading components. The oscillations in the force signal had a smaller amplitude compared to the experiments and the absorbed energy was underestimated. Furthermore, the frequency of the oscillations was somewhat higher in the simulation. Damping in the simulation is one possible reason for the

observed differences. Rate sensitivity of the applied materials and joints is another possible explanation. So far, only rate independent models were applied.

6. Conclusions

In this work, a novel test set-up is presented for validation of hybrid connector models between steel and aluminium components subjected to static and impact loading. The proposed components consisted of two hat profiles in steel and aluminium joined by adhesive bonding combined with SPR. The geometry of the components was determined by numerical simulations in order to focus the behaviour on the connections under various loading modes. Two specimen configurations were developed, one for normal and one for shear dominated loading. The chosen components were tested under static and dynamic loading conditions in a 3-point bending setup. Both specimen configurations yielded successive failure of the adhesive and the multiple SPR connections. Different displacement measurement techniques were applied to reveal the specimens behaviour, including digital image correlation. Up to date diagnostic techniques were used to ensure that the time and position of each failed connection could be identified precisely, which is essential in the validation of numerical connection models. The accurate manufacturing process of the component specimens ensured an excellent repeatability.

Results of the quasi-static and dynamic component tests were applied to validate idealised models of adhesively bonded and SPR connections. The deformation and failure behaviour of steel-aluminium components under quasi-static loading was represented well. The predicted force-displacement response of the normal loading component was in excellent agreement with the experiments. The force level was slightly underestimated for the shear loading component. Here, the adhesive connection had a larger influence because of the shear dominated loading. It is assumed, that the applied cohesive zone model underestimated the strength of the connection. In the simulations of the impact tests the overall behaviour seen in the experiments was captured quite well, even if the force level and thus the energy absorption was underestimated. The main reason for the underestimated force level is assumed to be caused by the fact that no rate effects are included in the modelling of the joints (adhesive and SPR connections) and base material. To establish rate dependent models for the adhesive and for the SPR connection model including calibration procedures requires new and extensive research and were thus not a part of the scope of the present work. However, the used models with a quasi-static calibration is assumed to give conservative results from an engineering point of view and can thus be used confidently in large scale shell analyses.

Declaration of Competing Interest

The authors declare that they have no known competing financial interests or personal relationships that could have appeared to influence the work reported in this paper.

Acknowledgements

The present work has been carried out with financial support from Centre of Advanced Structural Analysis (CASA), Centre for Research-based Innovation, at the Norwegian University of Science and Technology (NTNU), the Research Council of Norway through project no. 237885 (CASA) and BMW Group through its ProMotion programme for PhD students. The authors would like to acknowledge Mr.Trond Auestad and Mr. Tore Wisth for assistance with the various experimental programmes.

Appendix A. Modelling of the base materials

The isotropic, non-quadratic Hershey yield criterion [14] was applied to model the steel and aluminium material. The yield function f was defined as

$$f = \phi - (\sigma_0 + R) \leq 0 \tag{A.1}$$

and the equivalent stress φ was defined as

$$\phi = \left[\frac{1}{2}\left(|S_1 - S_2|^a + |S_2 - S_3|^a + |S_3 - S_1|^a\right)\right]^{\frac{1}{a}} \tag{A.2}$$

Here, S_1, S_2 and S_3 represent the principal deviatoric stresses. The curvature of the yield surface is defined by the exponent a. A value of $a = 6$ and $a = 8$ was chosen for the steel and aluminium material, respectively. The isotropic hardening variable R was defined by the Voce law

$$R = \sum_{i=1}^{N_R} Q_{Ri}\left(1 - exp\left(-\frac{\theta_{Ri}}{Q_{Ri}}\langle p - p_{start}\rangle\right)\right) \tag{A.3}$$

Appendix B. Modelling of the adhesive connection

The cohesive tractions $\boldsymbol{t}$ consist of the normal traction t_n and two shear tractions t_s and t_t.
The elastic domain was described by a linear uncoupled model.

$$\begin{Bmatrix} t_n \\ t_s \\ t_t \end{Bmatrix} = \begin{bmatrix} K_n & 0 & 0 \\ 0 & K_s & 0 \\ 0 & 0 & K_s \end{bmatrix} \begin{Bmatrix} \delta_n \\ \delta_s \\ \delta_t \end{Bmatrix} \tag{B.1}$$

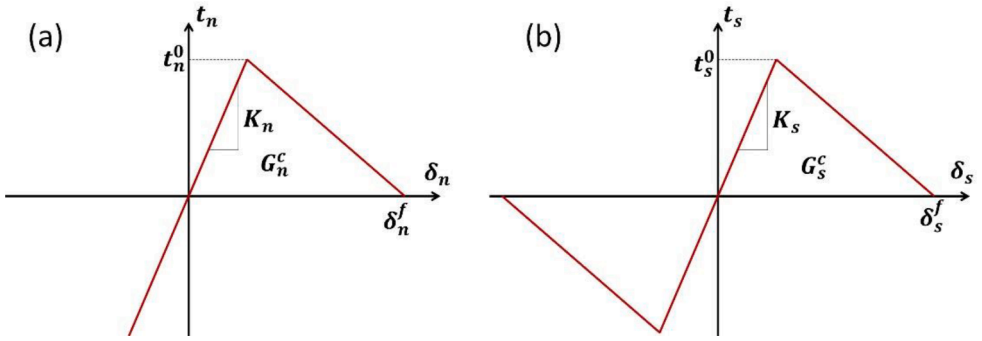

Fig. B.1. Triangular traction-separation law in a) normal and b) shear direction.

The normal stiffness K_n was defined by the elastic modulus E and the initial thickness of the cohesive element T_0.

$$K_n = \frac{E}{T_0},\ K_s = \frac{G}{T_0} \tag{B.2}$$

The shear stiffness K_s was defined by the shear modulus G. Here, the same value was applied in both shear directions. Damage initiation was defined by the maximum nominal stress criterion.

$$max\left\{\frac{\langle t_n \rangle}{t_n^0}, \frac{t_s}{t_s^0}, \frac{t_t}{t_s^0}\right\} = 1 \tag{B.3}$$

t_n^0 and t_s^0 define the maximum traction under pure normal and pure shear loading, respectively. The same critical value was applied for both shear directions. The Macaulay brackets in the damage criterion indicate, that damage cannot initiate under pure compression. A degradation of the material stiffness takes place after damage initiation. The degradation is controlled by the degradation variable d.

$$\boldsymbol{t} = (1-d)\boldsymbol{K\delta} \tag{B.4}$$

The evolution of d is defined by the triangular shape of the applied traction-separation law and the damage propagation criteria. Initially, the damage variable d takes on a value of 0 and a value of 1, when the damage propagation criteria is met. Damage propagation was defined by the linear power law form.

$$\frac{G_n}{G_n^C} + \frac{G_s}{G_s^C} + \frac{G_t}{G_s^C} = 1 \tag{B.5}$$

G_n, G_s and G_t define the current values of the energy release rate in the respective crack opening direction. The respective critical values G_n^C and G_s^C represent the area under the traction-separation curve and define the failure separations f_n and f_s. The same critical value G_s^C was applied in both shear directions.

Fig. B.1

Appendix C. Modelling of the SPR connection

The applied BUSHING connection type has a total of six components of relative motion as depicted in Fig. C.1.

$\boldsymbol{u}$ represents the connector relative displacements and rotations and $\boldsymbol{f}$ is the collection of the corresponding connector forces and moments. The connector behaviour defines the kinetic response regarding the available components of relative motion. The formulation allows to define an elastic and plastic response, as well as damage and failure.

Elasticity was described by a linear, uncoupled model. Here, the elastic behaviour can be defined individually for each component of relative motion. In this work, the elastic response was defined by the normal stiffness E_n and shear stiffness E_s. E_n was used for component 3 of relative motion while E_s was applied for components 1 and 2. The elastic response of the flexural rotations ur_1 and ur_2 (components 4 and 5) was assumed to be rigid.

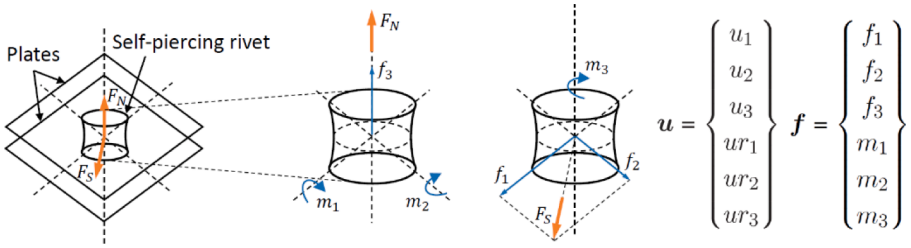

Fig. C.1. Connector forces, moments and derived components after [7].

No elastic stiffness was defined for the torsional rotation ur_3 (component 6). Usually, SPR connections can be easily rotated around the rivet axis, as negligible friction forces are the only resistance.

The formulation applied to describe the plastic behaviour of the connector is similar to formulations applied in metal plasticity. The connector potential P represents a scalar equivalent quantity, which is defined as a combination of the derived normal force F_N and derived shear force F_S.

$$P(\boldsymbol{f}) = \left[\left(\frac{F_N}{R_N}\right)^{\beta} + \left(\frac{F_S}{R_S}\right)^{\beta}\right]^{\frac{1}{\beta}} \tag{C.1}$$

The interaction between both quantities is defined by the parameter β. The contribution of F_N and F_S to the connector potential is weighted by the parameters R_N and R_S, respectively. The derived normal force F_N is defined as

$$F_N = \langle f_3 \rangle + \alpha\sqrt{m_1^2 + m_2^2} \tag{C.2}$$

Macaulay brackets are applied to only consider tension forces for component 3. The contributions of the flexural connector moments m_1 and m_2 are controlled by the coefficient α. The derived shear force F_S is defined as norm of the connector force component 1 and 2.

$$F_S = \sqrt{f_1^2 + f_2^2} \tag{C.3}$$

With the connector potential $P(\boldsymbol{f})$, the yield function was defined as

$$\Phi\left(\boldsymbol{f}, u_{pl,eq}\right) = P(\boldsymbol{f}) - F_y\left(u_{pl,eq}\right) \leq 0 \tag{C.4}$$

and associated plastic flow was assumed

$$\dot{\boldsymbol{u}}_{pl} = \dot{u}_{pl,eq}\frac{\partial \Phi}{\partial \boldsymbol{f}} \tag{C.5}$$

The yield force F_y was defined with respect to the equivalent plastic relative motion $u_{pl,eq}$. Isotropic hardening was assumed and the evolution of F_y was defined by three linear sections as shown in Fig. C.2.

The slope of the hardening curve was defined by the parameters F_y^{Ho}, F_y^{H1}, F_y^{H2} and $u_{pl,eq}^{H1}$, $u_{pl,eq}^{H2}$. Damage and failure of the connector were formulated as a function of the mode-mix ratio Ψ_m. It is defined by the ratio of the derived normal force F_N and the derived shear force F_S, as follows

$$\Psi_m = \frac{2}{\pi} tan^{-1}\left(\frac{F_N}{F_S}\right) \tag{C.6}$$

Consequently, the mode-mix ratio Ψ_m has a value of 1 for pure normal loading and a value of 0 for pure shear loading. Damage is included into the model by the damage variable d.

$$\boldsymbol{f} = (1-d)\boldsymbol{f}_{eff} \quad 0 \leq d \leq 1 \tag{C.7}$$

Prior to damage initiation, d takes on a value of 0. Connection failure takes place when d reaches a value of 1. The evolution of the damage variable d is shown in Fig. C.3a. Damage is initiated once the equivalent plastic relative motion takes on a user defined critical value $u_{pl,eq}^{I}$. The damage variable d approaches a value of 1 as the difference between $u_{pl,eq}^{I}$ and $u_{pl,eq}$ reaches a value of $\Delta u_{pl,eq}^{F}$.

Both, $u_{pl,eq}^{I}$ and $\Delta u_{pl,eq}^{F}$ can be provided as a function of the mode-mix ratio Ψ_m. In this work, the critical values were defined for three mode-mix ratios corresponding to the cross tests under tension, mixed-mode and shear loading. Values in between the user defined critical values were obtained from linear interpolation as illustrated in Fig. C.3b for $u_{pl,eq}^{I}$. For a more accurate description of the mixed-mode behaviour, values of $u_{pl,eq}^{I}$ and $\Delta u_{pl,eq}^{F}$ can be supplied for more than three mode-mix ratios. However, additional cross tests under different loading angles would be required for the calibration.

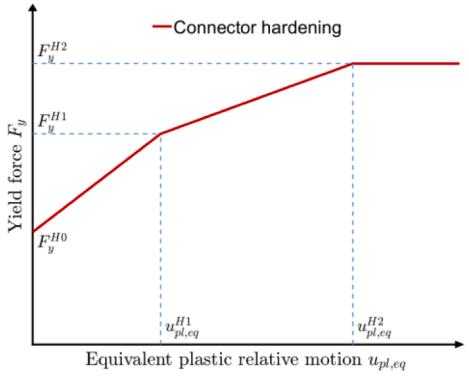

Fig. C.2. Connector hardening.

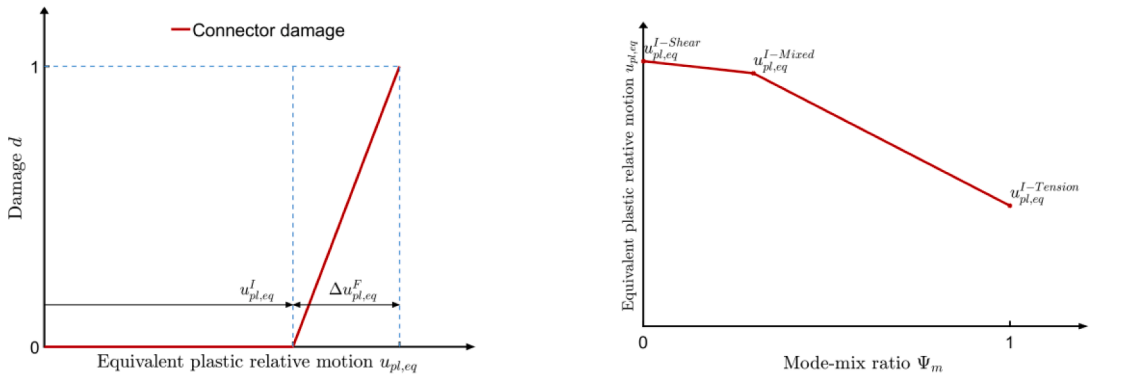

(a) Damage initiation and evolution

(b) $u^I_{pl,eq}$ as a function of the mode-mix ratio Ψ_m

Fig. C.3. Connector damage formulation.

References

[1] Oberkampf WL, Roy CJ. Verification and validation in scientific computing, press. Cambridge University; 2010.
[2] Pack K, Mohr D. Combined necking & fracture model to predict ductile failure with shell finite elements. Eng Fract Mech 2017;182:32–51.
[3] Costas M, Morin D, Hopperstad OS, Børvik T, Langseth M. Journal of the Mechanics and Physics of Solids A through-thickness damage regularisation scheme for shell elements subjected to severe bending and membrane deformations. J Mech Phys Solids 2019;123:190–206.
[4] Langrand B, Deletombe E, Markiewicz E, Drazétic P. Riveted joint modeling for numerical analysis of airframe crashworthiness. Finite Elem Anal Des 2001;38:21–44.
[5] Langrand B, Patronelli L, Deletombe E, Markiewicz E, Drazétic P. An alternative numerical approach for full scale characterisation for riveted joint design. Aerosp Sci Technol 2002;6:343–54.
[6] Combescure A, Delcroix F, Caplain L, Espanol S, Eliot P. A finite element to simulate the failure of weld points on impact. Int J Impact Eng 2003;28:783–802.
[7] Dassault Systemes. Abaqus 2017 online documentation. 2017.
[8] Porcaro R, Langseth M, Hanssen a, Zhao H, Weyer and H. Hooputra S. Crashworthiness of self-piercing riveted connections. Int J Impact Eng 2008;35(11):1251–66.
[9] Sønstabø JK, Morin and D, Langseth M. Testing and modelling of flow-drill screw connections under quasi-static loadings. J Mater Process Technol 2018;255:724–38.
[10] Reil M, Knoll O, Morin D, Langseth M. Testing of metal connections using adhesive bonding combined with self-piercing riveting. Technologies for economical and functional lightweight design. 2019. p. 167–73.
[11] Szlosarek R, Karall T, Enzinger N, Hahne C, Meyer N. Mechanical testing of flow drill screw joints between fibre-reinforced plastics and metals. Materialpruefung/Mater Test 2013;55:737–42.
[12] Sønstabø JK, Morin D, Langseth M. Macroscopic modelling of flow-drill screw connections in thin-walled aluminium structures. Thin-Walled Struct 2016;105:185–206.
[13] Sika Automotive GmbH. SikaPower-498. Crash resistant metal adhesive. Product Data Sheet. 2009.
[14] Hershey AV. The plasticity of an isotropic aggregate of anisotropic face centred. J Appl Mech 1954;21:241–9.
[15] Engler O, Schäfer C, Myhr OR. Effect of natural ageing and pre-straining on strength and anisotropy in aluminium alloy AA 6016. Mater Sci Eng 2015;639:65–74.
[16] Meschut G, Hahn O, Matzenmiller A, Mayer B. Experimentelle Kennwertermittlung und Simulation von strukturellen Klebverbindungen mit elastoplastischen und bruchmechanischen Kohäsivelementen, Schlussbericht Forschungsvorhaben P 957/422 ZN. Forschungsvereinigung stahlanwendung e. V. (FOSTA). Förderung der Industriellen Gemeinschaftsforschung (IGF); 2015.
[17] Fagerholt E. Field Measurements in Mechanical Testing Using Close-Range Photogrammetry and Digital Image Analysis. Doctoral Thesis. Norges teknisk-naturvitenskapelige universitet (NTNU); 2012.
[18] Hanssen AG, Auestad T, Tryland T, Langseth M. The kicking machine: a device for impact testing of structural components. Int J Crashworthiness 2003;8:385–92.
[19] Grimsmo EL, Clausen AH, Langseth M, Aalberg A. An experimental study of static and dynamic behaviour of bolted end-plate joints of steel. Int J Impact Eng 2015;85:132–45.
[20] Campilho R, Banea M, Neto JABP, Silva LFM. Modelling adhesive joints with cohesive zone models: effect of the cohesive law shape of the adhesive layer. Int J Adhes Adhes 2013;44(7):48–56.
[21] May M, Hesebeck O, Marzi S, Böhme W, Lienhard J, Kilchert S, et al. Rate dependent behavior of crash-optimized adhesives - Experimental characterization, model development, and simulation. Eng Fract Mech 2014;133(11).
[22] Chen Y, Clausen AH, Hopperstad OS, Langseth M. Stress–strain behaviour of aluminium alloys at a wide range of strain rates. Int J Solids Struct 2009;46:3825–35.
[23] Gruben G, Sølvernes S, Berstad T, Morin D, Hopperstad OS, Langseth M. Low-velocity impact behaviour and failure of stiffened steel plates. Mar Struct 2017;54:73–91.